We are IntechOpen,
the world's leading publisher of
Open Access books
Built by scientists, for scientists

4,800
Open access books available

122,000
International authors and editors

135M
Downloads

Our authors are among the

154
Countries delivered to

TOP 1%
most cited scientists

12.2%
Contributors from top 500 universities

WEB OF SCIENCE™

Selection of our books indexed in the Book Citation Index
in Web of Science™ Core Collection (BKCI)

Interested in publishing with us?
Contact book.department@intechopen.com

Numbers displayed above are based on latest data collected.
For more information visit www.intechopen.com

Small Scale Processes in the Solar Wind

Antonella Greco, Francesco Valentini and Sergio Servidio
Physics Department, University of Calabria, Rende (CS)
Italy

1. Introduction

The solar wind provides a fascinating laboratory for the investigation of a wide range of plasma physical nonlinear processes, such as, e.g., turbulence, intermittency, magnetic reconnection and plasma heating. One of the key aspects for a deep understanding of these phenomena is the plasma behaviour at small scales. This chapter is intended as a discussion forum on the role played by small scales in solar wind plasma dynamics and/or evolution. Processes occurring at large scales are anyhow responsible for the generation of small scale kinetic fluctuations and structures that in turn have important feedback on the global system evolution. In particular, we will focus our attention on two topics, namely magnetic reconnection and kinetic effects at short spatial scales.

For instance, magnetic reconnection occurring at non-MHD scales is linked to the small scale solar wind discontinuities. In particular, recent studies have shown that current sheets produced by turbulence cascade and discontinuities observed in the solar wind have very similar statistical properties and they are connected to intermittency.

Furthermore, the solar wind offers the best opportunity to study directly collisionless plasma phenomena and to attempt to address fundamental questions on how energy is transferred from fluid-large to small scales and how it is eventually dissipated. The processes by which energy is transferred from the fluid-scale inertial range into, ultimately, heating of ions and electrons are not well understood yet: there is growing evidence that multiple processes operate in the solar wind, either simultaneously or in different regimes. Kinetic effects (such as, for example, wave-particle resonant interaction) that presumably govern the short-scale dynamics are considered the best candidates to replace collisional processes in "dissipating" the energy at small wavelengths and in heating the plasma.

The aim of this chapter is to review the state of the art on these topics and their possible implications on space weather, both under theoretical and numerical standpoints, and comparing theoretical results with recent observations.

The chapter consists of two sections, at the end of which we give our conclusions.

2. Magnetic reconnection as an element of turbulence

Magnetic reconnection is a process that occurs in many astrophysical and laboratory plasmas (Moffatt, 1978). Systems like the solar surface (Parker, 1983), the magnetosphere (Sonnerup et al., 1981), the solar wind (Gosling & Szabo, 2008), and the magnetosheath (Retinò et al., 2007; Sundkvist et al., 2007) represent just some of the classical systems in which magnetic reconnection occurs. Another underlying common feature of the above systems is

the presence of turbulence (Bruno & Carbone, 2005), so a simultaneous description of both reconnection and turbulence is needed.

In the past 60 years, most of the theoretical effort has been addressed to the study of the basic physics of reconnection, concentrating on idealized two-dimensional (2D) geometries. Generally, these 2D models are characterized by a strong current density peak, where a magnetic *X*-type neutral point is found (Dungey, 1958). A well-known description of this process was provided by Sweet (Sweet, 1958) and Parker (Parker, 1957). In their work, employing conservation of mass, pressure balance and constancy of the electric field, the essential large scale dynamics of magnetic reconnection was described. In this configuration, a narrow layer called the "diffusion region" forms, and here the field-lines break and reconnect. This process produces a plasma flow into the layer, accompanied by an outflow along the neutral sheet.

In many cases the reconnecting system has been idealized as occurring in a limited spatial region, employing a "rigid-box" topology in which the magnetic field is often arbitrarily chosen to be straight at the inflow-side boundaries. Moreover, simplified "outflow" boundaries are employed. However, such idealized conditions rarely occur in nature, since plasmas may frequently experience turbulence (Bruno & Carbone, 2005). In turbulence, magnetic reconnection may behave in a less predictable way, departing considerably from rigid-box models.

We view reconnection as an element of turbulence itself: it would be difficult to envision a turbulent cascade that proceeds without change of magnetic topology. Furthermore, turbulence provides a natural boundary condition, as opposed to arbitrary (imposed) conditions. Although some suggestions have been made regarding both the general role of reconnection in magnetohydrodynamic (MHD) turbulence (Carbone et al., 1990; Dmitruk & Matthaeus, 2006; Matthaeus & Lamkin, 1986; Veltri, 1999)) and the impact of small scale turbulence on reconnection of large structures (Lapenta, 2008; Malara et al., 1992; Matthaeus & Montgomery, 1980; Matthaeus & Lamkin, 1986; Veltri, 1999)), only recently a quantitative study of reconnection in turbulence has been presented (Servidio et al., 2009; 2010a). In the scenario proposed in these papers, multiple-reconnection events are present in turbulence. The properties of these events depend on the local topology of the magnetic field and the local turbulence conditions.

Our ideas on magnetic reconnection have broad applications, and one of them is the turbulent solar wind. In the free solar wind, in fact, strong magnetic discontinuities are commonly observed (Burlaga, 1968; Tsurutani & Smith, 1979). These consist of rapid changes of the magnetic field, across narrow layers. It is natural to ask whether these discontinuities are related to the process of reconnection. In recent works by Greco et al. (2008; 2009); Servidio et al. (2011) a link between these rapid changes of the magnetic field and the presence of intermittent current sheets was proposed. In the present book chapter we retrace these ideas providing evidence that reconnection and discontinuities may be different faces of the same coin.

2.1 Overview on 2D MHD turbulence

The investigations described here are carried out in the limited context of incompressible 2D MHD, for which the turbulence problem, as well as the well-resolved reconnection problem, are already very demanding.
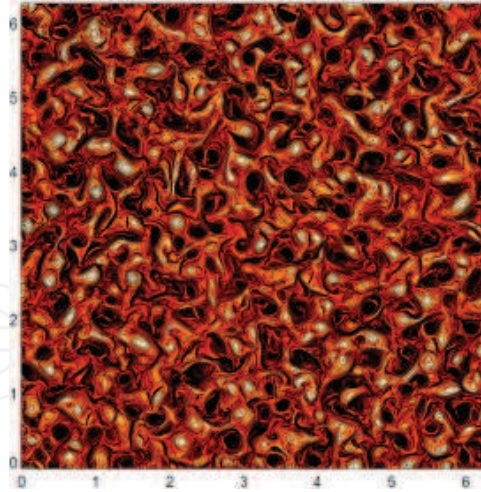
Fig. 1. Shaded contour of the current density j together with the line contours of the magnetic potential a at $t^* = 0.3$.

The 2D incompressible MHD equations can be written in terms of the magnetic potential $a(x, y)$ and the stream function $\psi(x, y)$. By choosing a uniform mass density $\rho = 1$, the equations read:

$$\frac{\partial \omega}{\partial t} = -\left(\boldsymbol{v} \cdot \boldsymbol{\nabla}\right) \omega + \left(\boldsymbol{b} \cdot \boldsymbol{\nabla}\right) j + R_\nu^{-1} \boldsymbol{\nabla}^2 \omega, \tag{1}$$

$$\frac{\partial a}{\partial t} = -\left(\boldsymbol{v} \cdot \boldsymbol{\nabla}\right) a + R_\mu^{-1} \boldsymbol{\nabla}^2 a, \tag{2}$$

where the magnetic field is $\boldsymbol{b} = \boldsymbol{\nabla} a \times \hat{\boldsymbol{z}}$, the velocity $\boldsymbol{v} = \boldsymbol{\nabla} \psi \times \hat{\boldsymbol{z}}$, the current density $j = -\boldsymbol{\nabla}^2 a$, and the vorticity $\omega = -\boldsymbol{\nabla}^2 \psi$. Eqs. (1)-(2) are written in Alfvén units with lengths scaled to L_0. The latter is a typical large scale length such that the box size is set to $2\pi L_0$. Velocities and magnetic fields are normalized to the root mean square Alfvén speed V_A and time is scaled to L_0/V_A. R_μ and R_ν are the magnetic and kinetic Reynolds numbers, respectively (at scale L_0.) The latter coefficients are reciprocals of kinematic viscosity and resistivity.

Eqs. (1)-(2) are solved in a periodic Cartesian geometry (x, y), using a well tested dealiased (2/3 rule) pseudo-spectral code. We employ a standard Laplacian dissipation term with constant dissipation coefficients. The latter are chosen to achieve both high Reynolds numbers and to ensure adequate spatial resolution. A detailed discussion of these issues has been given by Wan et al. (2010). We report on runs with resolution from 4096^2 up to 16384^2 grid points, reaching Reynolds numbers $R_\nu = R_\mu \sim 10000$. Time integration is second order Runge-Kutta and double precision is employed.

Considering a representation of the fields in the Fourier space, for a particular run, the energy is initially concentrated in the shell $5 \leq k \leq 30$ (wavenumber k in units of $1/L_0$), with mean value $E = \frac{1}{2}\langle |\boldsymbol{v}|^2 + |\boldsymbol{b}|^2 \rangle \simeq 1$, $\langle ... \rangle$ denoting a spatial average. Random uncorrelated phases are employed for the initial Fourier coefficients. The latter implies that the cross helicity, defined as $H_c = 1/2\langle \boldsymbol{v} \cdot \boldsymbol{b} \rangle$, is negligible. The kinetic and the magnetic energy at the beginning of the simulation are chosen to be equal.

We consider for the statistical analysis the state of the system at which the mean square current density $\langle j^2 \rangle$ is very near to its peak value. At this instant of time the peak of small scale turbulent activity is achieved.

When turbulence is fully developed, coherent structures appear. They can be identified as magnetic islands (or vortices). A typical complex pattern of 2D MHD turbulence is shown in Fig. 1, at high Reynolds numbers . In the figure is represented a contour plot of the current j, together with the in-plane magnetic field (line contour of a). The current density j becomes very high in narrow layers between islands.

In Fig. 2-(a), a zoom into the turbulent field is represented, showing that the current is bursty in space. This behavior of the current is related to the intermittent nature of the magnetic field (Mininni and Pouquet, 2009) and can be interpreted as a consequence of fast and local relaxation processes (Servidio et al., 2008). The probability distribution function (PDF) of the current density strongly departs from a Gaussian, as shown in Fig. 2-(b). These coherent structures interact non-linearly, merge, stretch, connect, attract and repulse each other. Reconnection is a major element of this complex interaction.
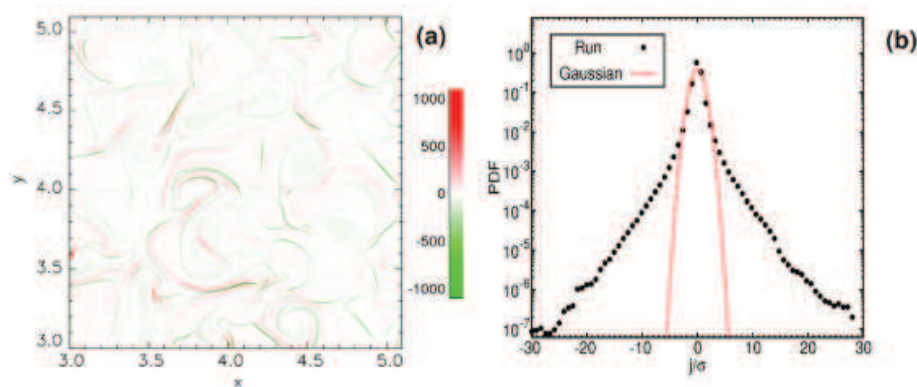

Fig. 2. (a) Shaded-contour of the current density j in a sub-region of the simulation box; (b) PDF of the current density, normalized to its variance, for high Reynolds number turbulence (black bullets). The Gaussian distribution is the red-dashed line.

2.2 Local reconnection events in turbulence

The reconnection rate of two islands is given by the electric field at the X-point. This is related to the fact that the magnetic flux in a closed 2D island is computed as the integrated magnetic field normal to any contour connecting the central O-point (maximum or minimum of a) with any other specified point. Choosing that point to be an X-point bounding the island, we find that the flux in the island is just $a(O - point)$, $-a(X - point)$. Flux is always lost at the O-point in a dissipative system, so the time rate of change of the flux due to activity at the X-point is

$$\frac{\partial a}{\partial t} = -E_\times = (R_\mu^{-1} j)_\times, \tag{3}$$

where $E_\times$ is an abbreviation for the electric field measured at the X-point (analogously for the current $j_\times$). Eq. (3) follows from the Ohm's law

$$\boldsymbol{E} = -\boldsymbol{v} \times \boldsymbol{b} + R_\mu^{-1} \mathbf{j}, \tag{4}$$

which in 2D involves only the out of plane component $E_z = -(\boldsymbol{v} \times \boldsymbol{b})_z + R_\mu^{-1} j$. Therefore, in order to describe the local processes of reconnection that spontaneously develop in turbulence
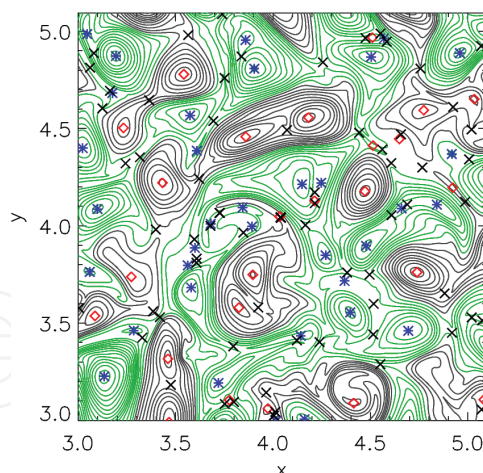
Fig. 3. Contour plot of the magnetic potential *a* with the position of all the critical points: *O*-points (blue stars for the maxima and red open-diamonds for the minima) and *X*-points (black ×).

we examine the topology of the magnetic potential studying the *Hessian matrix* of *a*, defined as

$$H_{i,j}^a(\boldsymbol{x}) = \frac{\partial^2 a}{\partial x_i \partial x_j}, \tag{5}$$

which we evaluate at the neutral points of the magnetic field. Further details on the methodology are provided in Servidio et al. (2010a). Here we briefly summarize the main steps of the analysis:

1. Identify critical points at $\boldsymbol{x}^*$, where $\boldsymbol{\nabla} a = 0$
2. Compute the Hessian matrix, given by Eq. (5), at $\boldsymbol{x}^*$
3. Compute eigenvalues λ_1 and λ_2 of $H_{i,j}^a(\boldsymbol{x}^*)$, with $\lambda_1 > \lambda_2$
4. Classify the critical point as maximum (both $\lambda_i < 0$), minimum (both $\lambda_i > 0$) and saddle points (or X-points) ($\lambda_1 \lambda_2 < 0$).
5. Compute eigenvectors at each X-point. The associated unit eigenvectors are $\hat{e}_s$ and $\hat{e}_l$, where coordinate *s* is associated with the minimum thickness δ of the current sheet, while *l* is associated with the elongation ℓ. Note that the local geometry of the diffusion region near each X-point is related to the Hessian eigenvalues $\lambda_1 = \frac{\partial^2 a}{\partial s^2}$ and $\lambda_2 = \frac{\partial^2 a}{\partial l^2}$.
6. According to Eq. (3), the reconnection rates are given by the electric field at the X-points. These rates are then normalized to the mean square fluctuation δb_{rms}^2, appropriate for Alfvènic turbulence.

In Fig. 3 we show the magnetic potential *a* with the critical point locations, obtained with the above procedure. In this complex picture the *X*-points link islands with different size and energy.

From a scaling analysis $\frac{\ell}{\delta} \simeq \sqrt{\lambda_R}$, where $\lambda_R = \left| \frac{\lambda_1}{\lambda_2} \right|$. In the case in which the reconnection is in a stationary state, the rate depends on the above aspect ratio λ_R, satisfying the scaling $E_\times \sim \frac{\ell}{\delta} \sim \sqrt{\lambda_R}$. In Fig. 4, a scatter plot of the reconnection rates against the aspect ratio λ_R is shown. There is a clear trend in this figure, showing that the expression for $E_\times$ is satisfied. This suggests that locally the reconnection processes depend on the geometry and that they therefore are in a quasi steady-state regime.
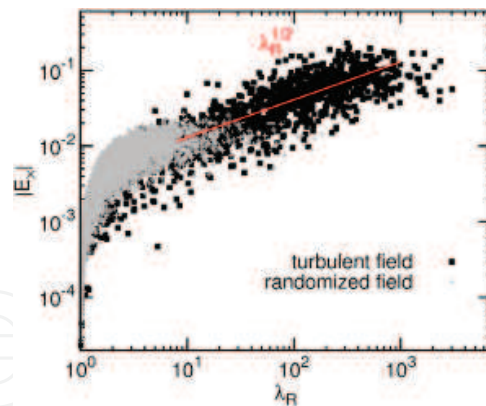
Fig. 4. Scatter plot (black full squares) of the reconnection rates *vs* the geometry of the reconnection region (ratio of the eigenvalues λ_R). The presence of a power-law fit (red line) demonstrates that there is a relation between the reconnection rate and the geometry of the diffusion region. The relative "randomized" reconnection rate is reported with (gray) crosses.

The approximate power-law scaling seen in Fig. 4 at larger values of λ_R suggests that the expression for $E_\times$ holds for the fastest reconnection events. The weaker reconnection events evidently follow a different scaling. We now show that the collection of slowly reconnecting (or even non-reconnecting) X-point regions is associated with a distribution of magnetic fields that is Gaussian. As described by Servidio et al. (2009; 2010a), we now employ a *phase-randomizing procedure*: the original turbulent field is compared with a hybrid field that has the same spectrum but random phases. The coherency of a turbulent pattern is, in fact, hidden in the phases of the Fourier expansion. Using this technique, one can distinguish between slow (Gaussian) and fast (non-Gaussian) reconnection events (Servidio et al., 2010a). As it can be seen from Fig. 4, the reconnection rates of the incoherent randomized magnetic field are on average much weaker than for the original case and they do not manifest any dependence on the aspect ratio of the eigenvalues. In fact the part of the distribution where we found the strongest reconnection sites and the scaling relation with aspect ratio is completely absent in the Gaussianized case. We would like to stress that phase-coherency analysis are widely used in the literature, and they are generally adopted to identify coherent structures (Hada et al., 2003; Sahraoui & Goldstein, 2010).

2.3 The link between magnetic reconnection and turbulence

Now we will take a closer look at the reconnection sites, trying to link them to the characteristic scales of MHD turbulence. Because of the complexity of the geometry we will focus only on the X-lines with higher reconnection rates, identified as described above. We need at this point to find a methodology to quantitatively characterize every reconnection region and extrapolate important information such as δ and ℓ. Since we know the ratio of the eigenvalues obtained from the Hessian matrix analysis, using $\frac{\ell}{\delta} \simeq \sqrt{\lambda_R}$, the problem reduces to find just one of these lengths, say δ.

We call $b_t(s)$ and $b_n(s)$ the normal and the tangential component of the magnetic field, respectively. These components are obtained by projecting the in-plane magnetic field into the system of reference given by $\{\hat{e}_l, \hat{e}_s\}$, that is $b_t = \hat{e}_l \cdot \boldsymbol{b}, b_n = \hat{e}_s \cdot \boldsymbol{b}$. Using the eigensystem of the Hessian matrix (λ_i and $\hat{e}_i$), together with local fit-functions, the up-stream magnetic field can be estimated, locally, for each reconnection region. Note that, the process of reconnection
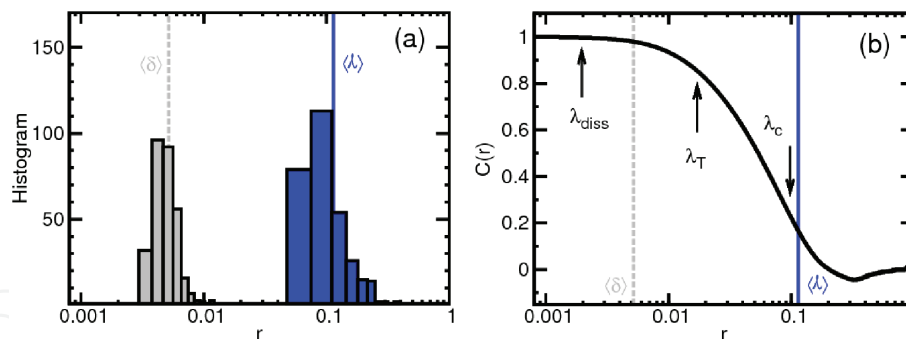
Fig. 5. (a) histograms of thicknesses (δ, gray bars) and elongations (ℓ, blue bars). Vertical lines are average values $\langle\delta\rangle$ (dashed gray) and $\langle\ell\rangle$ (full blue). (b) the magnetic field auto-correlation function (solid black line) is represented. The arrows (left to right) represent respectively: dissipation scale λ_{diss}, Taylor micro-scale λ_T and correlation length λ_C.

in turbulence is often asymmetric, so we define two upstream magnetic fields b_1 and b_2 (we suppressed subscript t).

The PDFs of δ and ℓ are reported in Fig. 5-(a), showing that they are well separated.

The present goal is to look for possible links between the reconnection geometry and the statistical properties of turbulence. In order to get more information about these associations we computed the auto-correlation function of the magnetic field. The correlation length is defined as $\lambda_C = \int_0^* C(r)dr$, where

$$C(\mathbf{r}) = \frac{\langle\boldsymbol{b}(\boldsymbol{x}+\mathbf{r})\cdot\boldsymbol{b}(\boldsymbol{x})\rangle}{\langle b^2\rangle}, \qquad (6)$$

where the direction of displacement r is arbitrary for isotropic turbulence in the plane, and the upper limit is unimportant if the distant eddies are uncorrelated. The correlation length λ_C is a measure of the size of the energy containing islands. The auto-correlation function is illustrated in Fig. 5-(b). In the same figure $\langle\delta\rangle$, $\langle\ell\rangle$ are reported as vertical lines for comparison. The dissipation length, at which the turbulence is critically damped, is defined as $\lambda_{diss} = R_\mu^{-\frac{1}{2}}\langle\omega^2 + j^2\rangle^{-\frac{1}{4}}$, while the Taylor micro-scale, a measure of mean-square gradients, is $\lambda_T = \sqrt{\frac{\langle|\boldsymbol{b}|^2\rangle}{\langle j^2\rangle}}$. The above lengths are represented in Fig. 5-(b).

It appears that the average elongation ℓ is strongly related to the correlation length where $C(r) \to 0$. For all simulations, we found that the values of diffusion layer thickness δ is distributed in the range between the Taylor scale and the dissipation scale, while the length ℓ, though broadly scattered, scales with λ_C (c.f. Fig. 5). The main features of this ensemble of reconnecting events, including the key length scales, are evidently controlled by the statistical properties of turbulence, setting the range of values of length and thickness of the diffusion regions according to the correlation length and the dissipation scale. Note that a correlation between diffusion width and dissipation was discussed experimentally by Sundkvist et al. (2007).

2.4 Applications to the turbulent solar wind

The statistical properties of reconnection have been investigated in the previous sections, leading to the conclusion that strong reconnection events can locally occur in 2D MHD
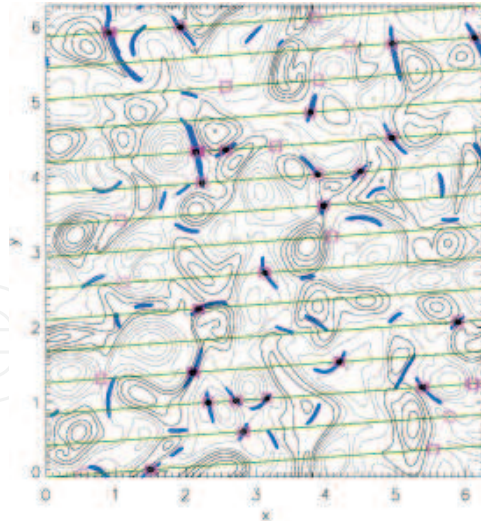
Fig. 6. Contour lines of the magnetic field (or line contour of *a*) together with the diffusion regions (blue shaded map), and with the one-dimensional path *s* (green solid line). On the same plot, the discontinuities identified by PVI technique with a threshold $\theta = 5$ in Eq. (8) (open magenta squares) are represented. Bullets (black) are discontinuities which correspond to reconnection sites.

turbulence. In this section we will review some of the main results about the link between solar wind discontinuities and local magnetic reconnection processes.

A well-known feature of solar wind observations is, in fact, the appearance of sudden changes in the magnetic field vector, defined as directional discontinuities (DDs), which are detected throughout the heliosphere (Burlaga, 1968; Ness & Burlaga, 2001; Neugebauer, 2006; Tsurutani & Smith, 1979). These changes are often seen at time-scales of 3 to 5 minutes, although similar discontinuities are seen at smaller time scales (Vasquez et al., 2007). In addition to identification based on characterization of discontinuities, coherent structures have also been identified using other approaches, such as wavelets (Bruno et al., 2001; Veltri & Mangeney, 1999) or phase coherency analysis (Hada et al., 2003; Koga et al., 2007; Koga & Hada, 2003).

One interpretation of magnetic discontinuities is that they are the walls between filamentary structures of a discontinuous solar wind plasma (Borovsky, 2006; Bruno et al., 2001; Burlaga,
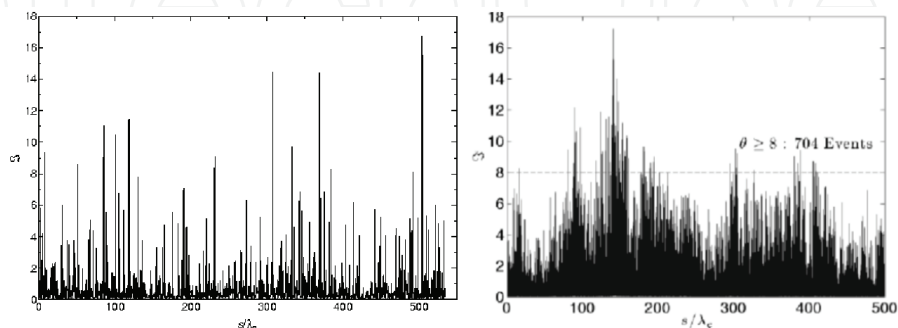

Fig. 7. Left: Spatial signal $\Im(\Delta s, \ell, s)$ (PVI) obtained from the simulation by sampling along the trajectory *s* in the simulation box, with $\Delta s \simeq 0.67 \lambda_{diss}$ and $\ell \simeq 535 \lambda_C$. Right: Same quantity obtained from solar wind data, with $\Delta s = 20$ s and $\ell \simeq 500 \lambda_C$.

1969), while another is that some strong discontinuities are fossils from the birth of the solar wind (Borovsky, 2008; Burlaga, 1968). An alternative possibility is that the observed discontinuities are the current sheets that form as a consequence of the MHD turbulent cascade (Matthaeus & Montgomery, 1980; Veltri, 1999)). Recent studies on magnetic discontinuities show that their statistical properties are very similar to distributions obtained from simulations of MHD turbulence (Greco et al., 2008; 2009). This line of reasoning argues that thin current sheets are characteristic coherent structures expected in active intermittent MHD turbulence (Mininni and Pouquet, 2009), and which are therefore integral to the dynamical couplings across scales. Therefore, solar wind discontinuities are one of the best applications of our theory of reconnection-in-turbulence.

In this perspective, one is led naturally to suspect that at least some of the current sheets that are a common feature of the solar wind at 1 AU may be participating in small-scale magnetic reconnection (Gosling & Szabo, 2008; Phan et al., 2010; Sundkvist et al., 2007), as well as inhomogeneous interplanetary plasma dissipation and heating (Leamon et al., 2000; Osman et al., 2011). To further establish the relationship between current sheets and small scale reconnection in turbulence, some quantitative connection is needed.

We have in mind the particular question: If one identifies a current sheet in turbulence, how likely is it to be also an active reconnection site? Here we show, using MHD simulation data, that methods for identifying intermittent current sheet-like structures, when quantified properly, can identify sets of structures that are likely to be active reconnection regions.

For the present statistical analysis we will consider a 4096^2 run. Anticipating possible applications to spacecraft data, we focus on properties of discontinuities that are recorded by magnetic field measurements at a single spacecraft in interplanetary space. We adopt a spacecraft-like sampling through the simulation domain [see Fig. 6 and Greco et al. (2008)], and we call s this trajectory. In particular, we can define a set whose elements consist of the segments of a trajectory that passes through any reconnection zone, identified by the *cellular automaton method* (Servidio et al., 2010a;b). In this way we can build a set of strong reconnection site encounters (*RS*) associated with a trajectory. Fig. 6 shows an example of reconnection sites together with the one-dimensional path s.

Interpolating the magnetic field data along the one-dimensional path s Greco et al. (2008), we can identify discontinuities (TDs) with the following procedure:

1. First, to describe rapid changes in the magnetic field, we look at the increments

$$\Delta \boldsymbol{b}(s, \Delta s) = \boldsymbol{b}(s + \Delta s) - \boldsymbol{b}(s), \tag{7}$$

   where Δs the spatial separation or lag. For this simulation we choose a small scale lag, $\Delta s \simeq 0.67 \lambda_{diss}$, which is comparable to the turbulence dissipation scales (see previous sections).

2. Second, employing only the sequence of magnetic increments, we compute the normalized magnitude

$$\Im(\Delta s, \ell, s) = \frac{|\Delta \mathbf{b}(s, \Delta s)|}{\sqrt{\langle |\Delta \mathbf{b}(s, \Delta s)|^2 \rangle_\ell}}, \tag{8}$$

   where $\langle \bullet \rangle_\ell = (1/\ell) \int_\ell \bullet ds$ denotes a spatial average over an interval of length ℓ, and Δs is the spatial lag in Eq. (7). The square of the above quantity has been called the *Partial Variance of Increments* (PVI) (Greco et al., 2008) and the method abbreviated as the PVI

Method	θ	# ITD	# IRS	efficiency (%)	goodness (%)
$\Im_1$	1	378	37	100	9.8
$\Im_5$	5	40	23	62.2	57.5
$\Im_8$	8	13	13	35.1	100

Table 1. First column: label of the method $\Im_\theta$. Second column: threshold θ imposed on PVI, cf., Eq.(9). Third column: #*ITD*, number of discontinuities identified by the method. Fourth column: #*IRS*, number of reconnection sites found by the method. Fifth column: #*IRS*/#*RS*, the relative efficiency of the method, identified reconnection sites as percent of all the reconnection sites present along the path. Last column: #*IRS*/#*ITD*, the relative goodness of the method, percent of identified reconnection events in set of identified discontinuities.

method. For the numerical analysis performed here $\ell \simeq 535\lambda_C$, where $\lambda_C = 0.18$ is the turbulence correlation length - a natural scale for computing averages.

The PVI time series, evaluated using Eqs. (7)-(8) is reported in Fig. 7. The illustration spans more than 500 correlation lengths. This spatial signal has been compared to a time signal measured by a ACE solar wind spacecraft, near 1 AU, over a period of about 20 days (right panel of the figure). In order to facilitate the comparison, we converted the time signal to a spatial signal, using the average velocity of the flow, and then normalized to a solar wind magnetic correlation length of 1.2×10^6 km.

The PVI increment time series is bursty, suggesting the presence of sharp gradients and localized coherent structures in the magnetic field, that represent the spatial intermittency of turbulence. These events may correspond to what are qualitatively called "tangential discontinuities" and, possibly, to reconnection events.

Imposing a threshold θ on Eq. (8), a collection of stronger discontinuities along the path s can be identified. That is, we select portions of the trajectory in which the condition

$$\Im(\Delta s, \ell, s) > \theta \tag{9}$$

is satisfied, and we will employ this condition to identify candidate reconnection sites. In Fig. 6, an example of the location of discontinuities along s, selected by the PVI method with a particular threshold θ, is shown. One can immediately see in Fig. 6 that there is an association, but not an identity, between the set of "events" identified using Eq. (9), and the encounters of the trajectory with reconnection regions. We will now study this association quantitatively using different values of threshold θ. To understand the physical meaning of the threshold θ, we recall Greco et al. (2008; 2009) that the probability distribution of the PVI statistic derived from a nonGaussian turbulent signal is empirically found to strongly deviate from the pdf of PVI computed from a Gaussian signal, for values of PVI greater than about 3. As PVI increases to values of 4 or more, the recorded "events" are extremely likely to be associated with coherent structures and therefore inconsistent with a signal having random phases. Thus, as θ is increased, stronger and more rare events are identified, associated with highly nonGaussian coherent structures.

We now adopt a procedure to count how many of the identified TDs [from Eq. (9)] are also reconnection sites (i.e., elements of the set *RS*), as follows: Every discontinuity is characterized by a starting and an ending point along the synthetic trajectory s. A set of discontinuities is identified, and a certain number of these discontinuities intersect reconnection regions. To automate the determination of the reconnection regions, we make use of a map (Servidio et al.,

2010b) that is generated using the cellular automaton procedure. The latter, in summary, is a 2D matrix that has 0 values in all cells outside of the diffusion regions, or values of 1 inside the diffusion regions. For this simulation, and for the selected trajectory (see Fig. 6), there are 37 reconnection sites along the path s. When at least one point of the identified candidate discontinuity overlaps with one point of the identified reconnection region, the event is counted as a "success". Otherwise the TD is not identified as an RS, and is a "failure". In the latter case the method is detecting a non-reconnecting, high-stress, magnetic field structure. However, such points are not associated with a region of strong reconnection, and therefore are not of interest in this analysis.

As an example, using $\theta = 5$ in Eq. (9), 40 discontinuities have been identified and 23 overlap a reconnection site and correspond to successful identification of a reconnection region. The goodness (quality) of this method can be defined as the number of the successes over the total number of identified discontinuities. For this example, the goodness is $\simeq 57.5\%$. An example of discontinuities, together with the reconnecting regions, is shown in Fig. 6.

Following the above procedure summarized by Eq. (9), we impose different threshold θ for the PVI signal. Each threshold characterizes a different set of discontinuities or "events", and we can label each algorithm as $\Im_\theta$. The parameters of different PVI-based algorithms are listed in Table 1, all of which use $\Im(\Delta s = 0.76\lambda_{diss}, \ell = 535\lambda_C)$. It can be seen that for higher values of θ an increasing fraction of the identified TDs corresponds to a reconnection site. That is, the goodness increases as the threshold θ is increased (Servidio et al., 2011).

For high θ, all the TDs correspond to reconnection sites. Once each reconnection site has been identified, the characteristic width δ' can be measured, as described by Servidio et al. (2011). For each TD captured by $\Im$, we measured each δ', and taking the average we obtained $\langle \delta' \rangle = 1.45 \times 10^{-2}$. From the 2D simulation, the average diffusion region thickness is $\langle \delta \rangle = 1.44 \times 10^{-2}$. The estimation $\langle \delta' \rangle$ is therefore in very good agreement with the average size of the diffusion region $\langle \delta \rangle$.

Other information such as the direction or orientation of each TD can be estimated. Using the assumption that the structures are one dimensional, in fact, there is a way to determine the normal vector to the discontinuity surface if single point measurements are used, namely the minimum variance analysis (MVA) technique (Sonnerup & Cahill, 1967). We will now test this technique, making use of the fact that we have a fully 2D picture of each RS from the simulation (see Fig. 6). In each TD detected with the PVI and expanded using the W-field, we compute the matrix $S_{ij} = \langle b_i b_j \rangle - \langle b_i \rangle \langle b_j \rangle$, where here $\langle \ldots \rangle$ denotes an average on the trajectory within the TD. Then we compute the eigenvalues (λ_1, λ_2) and the normalized eigenvectors $(\hat{\mathbf{n}}, \hat{\mathbf{t}})$, where λ_1 is the maximum eigenvalue and $\hat{\mathbf{n}}$ ($\hat{\mathbf{t}}$) is the normal (tangential) eigenvector. The values of the ratio λ_1/λ_2 is very large for all the discontinuities selected by $\Im_8$, that is $100 < \lambda_1/\lambda_2 < 10^7$. Another feature is that the normal component b_n is almost null and constant, while b_t is strongly changing sign.

2.4.1 An example from solar wind

We have computed the PVI time series using ACE 1 second resolution magnetic field data from the interval 2004 May 1 to 18 (Osman et al., 2011). The increment (Δs) is 20 seconds and the averaging interval in the denominator in Eq. (8) is the entire data period. The average velocity was around 400 km/s. In Fig. 7, the PVI time series is shown. In order to facilitate the comparison with simulation, we converted the time signal to a spatial signal, using the
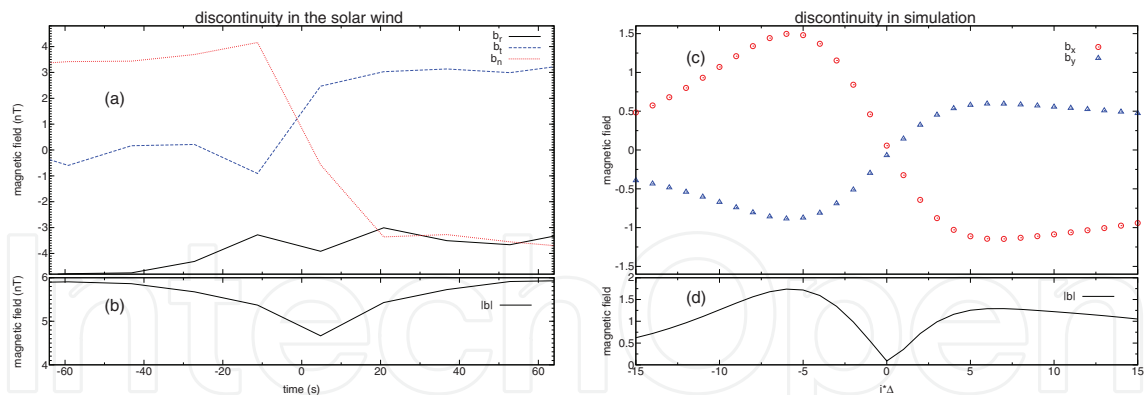
Fig. 8. Examples of discontinuities selected by the PVI method. Panel a: the three components of the magnetic field vector in solar wind data in the RTN reference frame; Panel b: magnitude of the magnetic field vector in solar wind data. The discontinuity, centered around zero, lasts few tens seconds. Panel c: the two components of the magnetic field vector in simulation data; Panel d: magnitude of the magnetic field vector in simulation data. Δ is the resolution data.
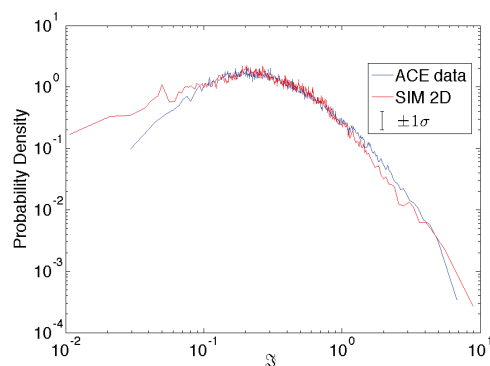

Fig. 9. Probability density function of the spatial signal $\Im$ (PVI) obtained from ACE measurements (blue line) and simulation (red line). The error bar $\pm \sigma$ is displayed in the legend and the value of σ is the expected fractional error in the PDF due to counting statistics.

average velocity of the flow, and then normalized to a solar wind magnetic correlation length of 1.2×10^6 km. Imposing a threshold $\theta > 8$ on Eq. (8), 704 events are identified. One of these TDs is illustrated in Fig. 8 along with an example of TD from the 2D MHD simulation. Finally, in Fig. 9, we show the probability distribution functions of the PVI signal for both the observational and simulation data. The comparison tells us that there is a great similarity within the errors. In general, we suggest that the methods developed here may have many applications to the the solar wind data, where the coexistence of turbulence and magnetic reconnection cannot be discarded.

2.5 Conclusion

In these sections we have assembled a digest of recent works that has examined magnetic reconnection, not as an isolated process that occurs in idealized, controlled conditions, but as a necessary ingredient in the complex nonlinear dynamical process that we call turbulence. Much of the progress in three dimensional (3D) non-steady or turbulent reconnection has been either experimental (e.g., Ren et al., 2005) or in a 3D numerical setup that is in effect

nearly 2D (Daughton et al., 2011). It is noteworthy that the fully 3D case is substantial more complex and less understood, both theoretically (Priest and Pontin, 2009), and in numerical simulations (Dmitruk & Matthaeus, 2006). However, for weakly 3D setups, it has been amply confirmed that turbulence effects (Matthaeus & Lamkin, 1986; Servidio et al., 2009) persist (Daughton et al., 2011). While important aspects of the physics of reconnection revealed in the 2D paradigm can carry over to 3D, it is likely also that there are essential physical effects that occur only in a strongly 3D system or with kinetic effects at the small scales.

Most of the progress reviewed here has been in the context of nonlinear dynamics of magnetic reconnection in turbulence, investigated through direct numerical simulations of decaying 2D MHD. The reconnection is spontaneous but locally driven by the fields and boundary conditions provided by the turbulence.

The turbulent cascade produces a distribution of reconnecting islands. Computing the electric field at the X-points, we see that turbulence produces a broad range of reconnection rates. In addition, the strongest reconnection rates vary in proportion to ℓ/δ, the aspect ratio of the reconnection sites. This scaling appears superficially to differ greatly from classical laminar theories (Parker, 1957; Sweet, 1958). These results explain how rapid reconnection occurs in MHD turbulence in association with the most intermittent non-Gaussian current structures, and also how turbulence generates a very large number of reconnection sites that have very small rates.

In contrast to laminar reconnection models that provide a single predicted reconnection rate for the system, turbulent resistive MHD gives rise to a broad range of reconnection rates that depend on local turbulence parameters. Many potential reconnection sites are present, but only a few are selected by the turbulence, at a given time, to display robust reconnection electric fields. In this way, the present problem differs greatly from studies of reconnection that assume that it occurs in isolation or as a spontaneous process.

We have seen that reconnection becomes an integral part of turbulence, as suggested previously (Carbone et al., 1990; Matthaeus & Montgomery, 1980). This perspective on reconnection in turbulence that we have reviewed here seems to be potentially very relevant to space and astrophysical applications such as the turbulent solar wind (Gosling & Szabo, 2008; Sundkvist et al., 2007). On the basis of the current results, we would expect to find in the turbulent corona and solar wind a broad distribution of size of interacting islands, with a concomitantly broad distribution of reconnection rates. Furthermore a useful extension will be to employ models that are suited to low collisionality plasmas, where for example anomalous resistivity, or kinetic effects, may be important.

3. The electrostatic character of the high-frequency energy spectra in the solar wind

The interplanetary medium, the bubble of plasma that is generated by the Sun and that fills the Heliosphere, is known to be hotter than expected in an expanding plasma. Understanding how energy from the Sun can be dissipated into heat in such a collision-free system represents a top priority in space physics. The Sun injects energy into the Heliosphere through large wavelength fluctuations (Alfvén waves). This energy is then channeled towards short scales through a turbulent cascade until it can be transferred to the plasma particles in the form of heat.

The study of the short-wavelength region of the solar-wind turbulent cascade represents nowadays a subject of active interest in space plasma physics. Many experimental works (Alexandrova et al., 2009; Bale et al., 2005; Sahraoui et al., 2009), focused on the analysis of the solar-wind data from spacecraft, aim to investigate how the energy of the large-scale Alfvénic fluctuations can be transferred towards short scales and eventually turned into heat. Within this scenario a crucial point is the identification of the fluctuations that channel the energy from large to short wavelengths along the turbulent cascade.

Long ago it has been shown (Matthaeus et al., 1986) that in the solar wind the Magnetohydrodynamics fluctuations are mainly composed by two populations: the first one with wavevectors predominantly perpendicular to the ambient magnetic field (2D turbulence) and the second one with wavector aligned to the background field (slab turbulence). As recently discussed, for example, by means of Gyrokinetics simulations (Howes et al., 2008)), 2D turbulence seems to give rise, at length scales below the ion-gyro scale, to transverse electromagnetic fluctuations whose features are consistent with the so-called kinetic Alfvén waves. These results provide a significant interpretation to solar-wind observations from the Cluster spacecraft (Sahraoui et al., 2009) in which a quasi-two-dimensional cascade into kinetic Alfvén waves seems to be identified. This cascade represents then a channel available to bring energy from large to small scales.

The second population (slab turbulence) can produce a second channel, in the form of electrostatic fluctuations, for the transport of energy towards small scales. The first insights into the nature of this kind of phenomenon date back to the late seventies, when solar wind measurements from the Helios spacecraft (Gurnett & Andreson, 1977; Gurnett & Frank, 1978; Gurnett et al., 1979) have shown that the high-frequency (few kHz) range of the solar wind turbulent cascade is characterized by the presence of a significant level of electrostatic activity identified as ion-acoustic waves propagating parallel to the ambient magnetic field. The energy level of these fluctuations shows a certain correlation to the electron to proton temperature ratio T_e/T_p and surprisingly survives even for small values of T_e/T_p, for which linear Vlasov theory (Krall & Trivelpiece, 1986) predicts strong Landau dissipation. The propagation of these fluctuations seems to be correlated to the generation of non-Maxwellian proton velocity distributions that display the presence of beams of accelerated particles in the direction of the ambient magnetic field, moving with mean velocity close to the local Alfvén speed. More recent data from the WIND (Lacombe et al., 2002; Mangeney et al., 1999) and the CLUSTER (Pickett et al., 2004) spacecraft allowed to analyze in more detail the features of this electrostatic activity at high frequency in the solar wind. Subsequent experimental space observations confirmed that the particle velocity distributions show a general tendency to depart from the Maxwellian equilibrium configuration, displaying temperature anisotropy (Hellinger at al., 2006; Holloweg & Isenberg, 2002; Marsch et al., 2004) and generation of field-aligned accelerated beams (Heuer & Marsch, 2007; Marsch et al., 1982; Tu et al., 2004)).

These experimental results support the idea that kinetic effects are at work in the solar wind plasmas at short spatial scale lengths, but many aspects of the experimental evidences discussed above still need a convincing physical interpretation: (i) how electrostatic fluctuations of the ion-acoustic type can survive against damping in the case of cold electrons ($T_e \simeq T_p$), (ii) why the mean velocity of the field-aligned beam of accelerated protons is commonly observed to be of the order of the local Alfvén speed.

Recently, many authors used kinetic numerical simulations to reproduce the solar-wind phenomenology described above, that is the generation of longitudinal proton-beam velocity distributions associated with the propagation of electrostatic fluctuations. In particular, Araneda et al. (2008) presented one-dimensional hybrid Particle In Cell (PIC) simulations in which ion-acoustic (IA) fluctuations, generated through parametric instability of monochromatic Alfvén-cyclotron waves, produce field-aligned proton beams during the saturation phase of the wave-particle interaction process. More recently, Matteini et al. (2010) analyzed in detail the relationship between the kinetic aspects of the parametric instability of Alfvén waves (in the case of monochromatic pump waves and of a spectrum of waves) and the evolution of the proton distribution functions, again making use of numerical PIC simulations in hybrid regime.

The parametric instability of left-handed polarized Alfvén waves, considered in the papers referenced above, is efficient in producing IA fluctuations in regimes of low values of the proton plasma beta β_p (Longtin & Sonnerup, 1986) and for large values of the electron to proton temperature ratio, since IA waves are heavily Landau damped for small T_e/T_p (Krall & Trivelpiece, 1986). >From the solar wind observations, the mean velocity of the longitudinal proton beam is typically of the order of the local Alfvén speed. As discussed by Araneda et al. (2008); Matteini et al. (2010), the IA fluctuations, produced through parametric instability, trap resonant protons and dig the particle velocity distribution in the vicinity of the wave phase speed, thus creating the field-aligned beam; it follows that, in order to generate a beam with a mean velocity close to V_A through this mechanism, the phase velocity $v_\phi^{(IA)}$ of the IA fluctuations must be of the same order of V_A [$v_\phi^{(IA)} \simeq V_A$]. Taking into account that the phase speed of the IA waves is $v_\phi^{(IA)} \simeq \sqrt{T_e/m_p}$, the condition necessary to produce a beam with mean velocity of the order of V_A is $T_e/m_p \simeq V_A^2 \Rightarrow T_e/T_p \simeq m_p V_A^2/T_p \simeq 1/\beta_p$, or, equivalently, $(T_e/T_p)\beta_p \simeq 1$. Large values of T_e/T_p, needed for IA fluctuations to survive against Landau damping, require low values of β_p to keep this condition valid. This range of parameters is unusual for the solar wind plasma, where the electron to proton temperature ratio varies in the range $0.5 < T_e/T_p < 4$ (Schwenn & Marsch, 1991), while β_p is typically of order unity. Moreover, it is not clear why the electrostatic activity in the high frequency region of the solar-wind energy spectra is observed even at low values of T_e/T_p and why the secondary proton beam has a mean velocity always of the order of the local Alfvén speed.

Beside the numerical simulations described above, a newly developed Eulerian hybrid Vlasov-Maxwell code (Valentini et al., 2007)) has been used to propose a different mechanism for the generation of the proton-beam distributions associated to the short-scale electrostatic activity in the solar wind. This code solves numerically the Vlasov equation for the protons, while the electrons are considered as a fluid; a generalized Ohm's equation for the electric field, where the Hall term and the electron inertia terms are retained, is integrated. The Faraday equation, the equation for the curl of the magnetic field (where the displacement current is neglected) and an isothermal equation of state for the electron pressure close the set of equations. The quasi-neutrality assumption is considered.

These hybrid Vlasov-Maxwell simulations in 1D-3V phase space configuration (one dimension in physical space and three dimensions in velocity space) (Valentini et al., 2008); Valentini & Veltri, 2009)) were focused on a physical situation where Magnetohydrodynamics turbulence evolves to a state where a significant amount of energy is stored in

longitudinal wavevector modes (slab turbulence) (Carbone et al., 1995; Dobrowolny et al., 1980; Matthaeus et al., 1986). The turbulent energy cascade is triggered by nonlinear wave-wave interaction of large scale ion-cyclotron (IC) waves. The numerical results from these simulations gave evidence that for large values of the electron to proton temperature ratio ($T_e/T_p = 10$) the tail of the turbulent cascade at short scales is characterized by the presence of electrostatic fluctuations, propagating in the direction of the mean magnetic field. The Fourier $k - \omega$ spectrum of the numerical signals revealed that, beside the IA branch, a new branch of waves with phase speed close to the proton thermal speed and with acoustic dispersion relation appears. These new waves have been dubbed ion-bulk (IBk) waves. It has been shown that the diffusive plateaus, created in the longitudinal proton velocity distribution through resonant interaction of protons with IC waves (Heuer & Marsch, 2007; Kennel & Engelmann, 1966), are responsible for the excitation of the IBk waves. This phenomenology leads to the generation of a beam of accelerated protons in the direction of the ambient field with mean velocity close to V_A. These results have been confirmed through hybrid-Vlasov simulations in 2D-3V phase space configuration (Valentini et al., 2010)). Moreover, in 2011 Valentini et al. (2011)) the existence of the IBk waves has also been demonstrated by means of electrostatic kinetic simulations, in which an external driver electric field is used to create a longitudinal plateau in the proton velocity distribution.

Here, we review the main results of a series of 1D-3V hybrid Vlasov-Maxwell simulations (in physical situation of slab turbulence), in which the development of the turbulent cascade towards short spatial lengths is investigated in terms of the electron to proton temperature ratio. This analysis allows to demonstrate that the electrostatic fluctuations at short wavelengths, generated as the result of the turbulent cascade, can last in typical conditions of the solar-wind plasma, that is even for low values of T_e/T_p. Moreover, through our numerical simulations we describe a physical mechanism leading to the generation of a field-aligned proton beam with mean velocity close to the Alfvén speed that works even for small values of T_e/T_p provided the proton plasma beta is of order unity.

3.1 Numerical results

As discussed in the Introduction, we numerically follow the kinetic dynamics of protons in 1D-3V phase space configuration (periodic boundary conditions are imposed in physical space). In the following, times are scaled by the proton cyclotron frequency Ω_{cp}, velocities by the Alfvén speed $V_A = B_0/\sqrt{4\pi\rho}$ (B_0 being the magnetic field and ρ the mass density), lengths by the proton skin depth $\lambda_p = V_A/\Omega_{cp}$ and masses by the proton mass m_p.

We assume that at $t = 0$ the plasma has uniform density and is embedded in a background magnetic field $\mathbf{B}_0 = B_0\mathbf{e}_x$, with superposed a set of Alfvén waves, circularly left-hand polarized in the plane perpendicular to the mean magnetic field and propagating along it. The explicit expressions for the velocity and magnetic perturbations [$\delta u_y(x)$, $\delta u_z(x)$, $\delta B_y(x)$ and $\delta B_z(x)$] were derived from the linearized two-fluid equations (Valentini et al., 2007)). The first three modes in the spectrum of velocity and magnetic perturbations are excited at $t = 0$, in such a way that the maximum perturbation amplitude is $A = 0.5$. No density disturbances are imposed at $t = 0$. The initial Maxwellian ion distribution is $f(x, \mathbf{v}, t = 0) = A(x)\exp\left[-(\mathbf{v} - \delta\mathbf{u})^2/\beta_p\right]$, where $\beta_p = 2v_{tp}^2/V_A^2$ ($v_{tp} = \sqrt{T_p/m_p}$ being the proton thermal speed and T_p the proton temperature); $A(x)$ is such that the velocity integral of f gives the equilibrium density $n_0 = 1$. The value of the proton plasma beta is fixed at
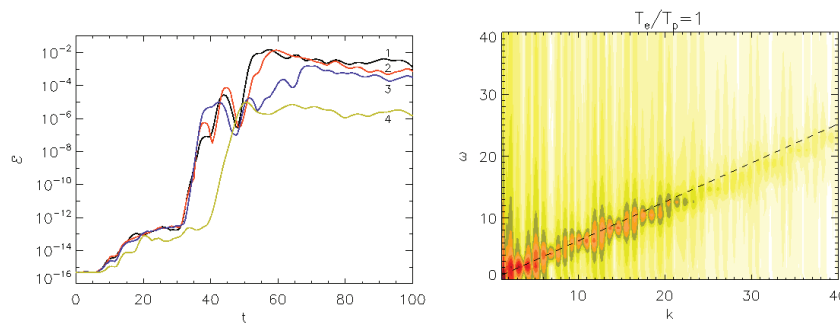
Fig. 10. Left: Time evolution of $\mathcal{E}$ for $T_e/T_p = 10$ [black line (1)], $T_e/T_p = 6$ [red line (2)], $T_e/T_p = 3$ [blue line (3)] and $T_e/T_p = 1$ [green line (4)]; right: k-ω spectrum of the parallel electric energy for the case $T_e/T_p = 1$.

$\beta_p = 0.5$ (the proton thermal velocity is $v_{tp} = 0.5$) and the system evolution is analyzed for different values of the electron to proton temperature ratio ($T_e/T_p = 1, 3, 6, 10$). The mass ratio is $m_e/m_p = 1/1836$. The length of the physical domain is $L_x \simeq 40.2$ (the fundamental wave number is $k_1 = 2\pi/L_x \simeq 0.156$), while the limits of the velocity domain in each direction are fixed at $v^{max} = 5v_{tp}$. We use 2048 gridpoints in physical space, and 51^3 in velocity space and a time step $\Delta t = 10^{-3}$. The simulation is carried up to $t = 400$.

The nonlinear three-wave interactions at large scales trigger the turbulent energy cascade. When the energy is carried at frequencies close to Ω_{cp}, the resonant interaction of the protons with the IC waves produces the formation of a diffusive plateau in the longitudinal velocity distribution in the vicinity of the phase speed $v_\phi^{(IC)}$ of the IC waves (Valentini et al., 2008)). For parallel propagating IC waves one has $v_\phi^{(IC)} \simeq V_A$ for frequencies smaller than Ω_{cp} (or, equivalently for small wave numbers) and $v_\phi^{(IC)} < V_A$ for frequencies close to Ω_{cp}. If β_p is of order unity one gets $v_\phi^{(IC)} \leq V_A \simeq v_{tp}$, this means that the diffusive plateau is created in the vicinity of the proton thermal speed, or, equivalently, in the bulk of the proton velocity distribution.

When the proton velocity distribution is flattened in the vicinity of v_{tp}, the IBk waves can be excited (Valentini et al., 2008; Valentini & Veltri, 2009; Valentini et al., 2011)) and the energy is transferred from large to short wavelengths along the IBk channel. From the analysis of the numerical results, one realizes that in the range of large wavenumbers, say $k > 10\lambda_p^{-1}$, the parallel electric energy is the dominant component of the energy spectrum, this meaning that the tail at short wavelengths of the turbulent cascade is characterized by the presence of electrostatic activity. On the left in Fig. 10, we report in semi-logarithmic plot the early time evolution ($0 < t < 100$) of the longitudinal electric energy at small scales evaluated as $\mathcal{E}(t) = \sum_k |E_{k_x}|^2$ with $k > 10\lambda_p^{-1}$. The black line (1) corresponds to a simulation with $T_e/T_p = 10$, the red line (2) to $T_e/T_p = 6$, the blue line (3) to $T_e/T_p = 3$ and the green line (4) to $T_e/T_p = 1$. It is clear from this figure that, during the system evolution, $\mathcal{E}$ displays a sudden exponential growth and then a saturation phase. We notice that for $T_e/T_p = 1$ the exponential growing phase is somewhat delayed with respect to the case with $T_e/T_p = 10, 6, 3$.

The physical mechanism responsible for this exponential growth consists in an instability process of the beam-plasma type (Valentini et al., 2011)): the resonant interaction of protons with IC waves of large amplitude creates regions of positive slope (small bumps) instead of flat plateaus in the longitudinal proton velocity distribution at v_{tp}; this triggers the growth of high wavenumbers electric field components in parallel propagation with phase speed comparable to v_{tp}. As recently shown by Valentini et al. (2011)), the IBk waves can be excited only when a plateau in the longitudinal proton velocity distribution is generated in the vicinity of v_{tp}. In the present hybrid Vlasov-Maxwell simulations, a diffusive longitudinal plateau is generated at $v_\phi^{(IC)} \leq V_A$, as the result of the resonant interaction between IC waves and protons; when β_p is of order unity one gets $v_\phi^{(IC)} \leq V_A \simeq v_{tp}$, this meaning that the plateau can be produced at v_{tp} and the IBk waves can be excited. We considered different simulations with $0.5 \leq \beta_p \leq 2$ obtaining the same qualitative system evolution. On the other hand, the mechanism described above cannot work for small values of β_p.

The growth of $\mathcal{E}$ corresponds to the excitation of electrostatic fluctuations at high wavenumbers. The energetic level of these fluctuations after the saturation of the exponential growth depends on T_e/T_p; the largest saturation value of $\mathcal{E}$ is found for $T_e/T_p = 10$, but even at $T_e/T_p = 1$ a significant level of fluctuations is recovered. On the right of Fig. 10 we show the k-ω spectrum of the parallel electric energy for the simulation with $T_e/T_p = 1$. The acoustic branch visible in this spectrum is the branch of the IBk waves with phase speed $v_\phi^{(IBk)} \sim 1.2 v_{tp}$ (black dashed line in the figure). As shown by Valentini et al. (2008)); Valentini & Veltri (2009)), for a simulation with $T_e/T_p = 10$ the branch of IA waves also appears in the k-ω spectrum of the parallel electric energy beside the IBk branch. For such a large value of T_e/T_p, the IA fluctuations generated in the early stage of the system evolution by ponderomotive effects can survive against Landau damping up to the end of the simulation. Nevertheless, here we show that, when decreasing the value of T_e/T_p these IA waves are Landau damped quite soon and disappear from the k-ω spectrum, as it is clear from the right plot of Fig. 10 for $T_e/T_p = 1$.
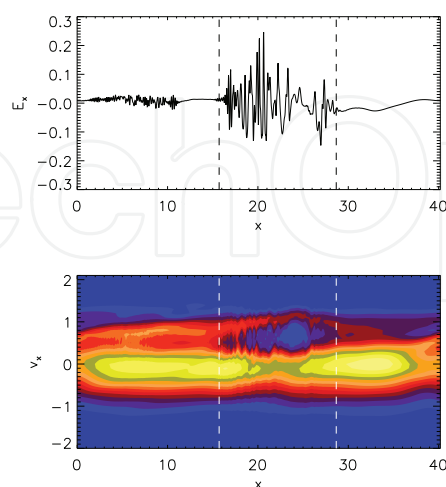

Fig. 11. At the top: parallel electric field E_x versus x at $t = 100$; at the bottom: longitudinal phase space level lines of the proton distribution function at $t = 100$.
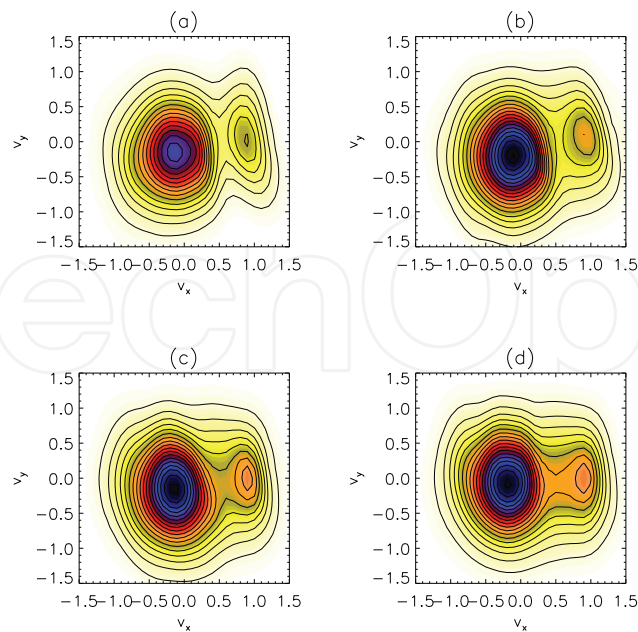
Fig. 12. v_x-v_y contour lines of the proton distribution function integrated over v_z and averaged over x in the region corresponding to the trapped particle population, for $T_e/T_p = 1$ (a), $T_e/T_p = 3$ (b), $T_e/T_p = 6$ (c) and $T_e/T_p = 10$ (d).
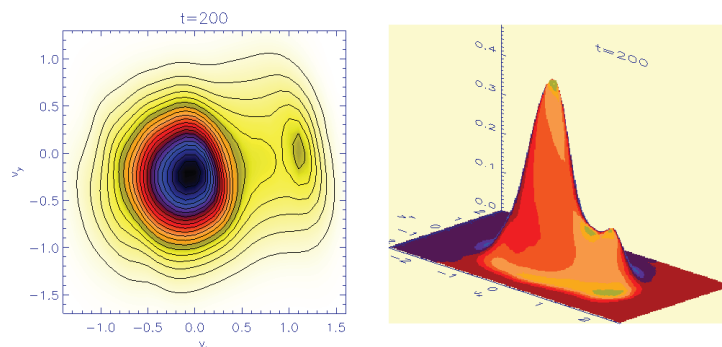

Fig. 13. v_x-v_y contour lines (left) together with the surface plot (right) of the proton distribution function integrated over v_z and averaged over x in the region corresponding to the trapped particle population, in the case $T_e/T_p = 10$, at $t = 200$.

In the top frame of Fig. 11 we show the electric field E_x as a function of x at the end of the simulation for the case $T_e/T_p = 3$. As it is easily seen from this plot, a short-scale localized wavepacket is generated as the results of the phenomenology described above. We point out that for simulations with $T_e/T_p = 1, 6, 10$ we observed the generation of similar structures, with amplitude that depends on T_e/T_p (the largest amplitude is found for $T_e/T_p = 10$). These electrostatic signals propagate with phase velocity $v_\phi \simeq v_{tp}$ (independent on T_e/T_p) and trap resonant protons moving with velocity close to v_{tp}. This is shown in the bottom frame of Fig. 11, where the contour lines of the longitudinal phase space proton distribution function are represented at $t = 100$ for $T_e/T_p = 3$; the region of trapped particles is delimited in space by the vertical white dashed lines and moves with mean velocity close to $v_{tp} = 0.5$.

In order to show how the generation of a trapped particle population affects the proton velocity distribution, in Fig 12 we report the v_x-v_y level curves of f, integrated over v_z and averaged over x in the interval corresponding to the trapping region (see the white dashed lines at the bottom in Fig. 11), for $T_e/T_p = 1$ (a), $T_e/T_p = 3$ (b), $T_e/T_p = 6$ (c) and $T_e/T_p = 10$ (d), at $t = 100$. In each plot of Fig. 12 a beam of accelerated protons is generated in the direction of the ambient magnetic field. We point out that the mean velocity of this secondary beam (of the order of $V_A = 1$) as well as its height is independent on the value of T_e/T_p. We emphasize that this numerical evidence provides a reliable interpretation of the physical mechanism leading to the generation of field-aligned beams of protons in the solar wind velocity distributions. The beam of accelerated particle in the direction of the mean magnetic field is very stable and long lived structure in time as wine show in Fig. 13, where the v_x-v_y contour lines of the proton distribution (left) together with a surface plot of the same distribution are displayed for the case $T_e/T_p = 10$ at $t = 200$.
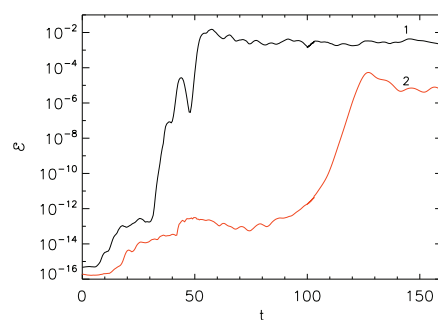

Fig. 14. Time evolution of $\mathcal{E}$ for a simulation with $T_e/T_p = 10$, for $A = 0.5$ [black line (1)], $A = 0.2$ [red line (2)].

As a next step, we consider a new simulation with $T_e/T_p = 10$ in which we decreased the amplitude of the initial Alfvénic perturbations to the value $A = 0.2$ and compare the results of this new simulation with those of the old simulation with $A = 0.5$. In Fig. 14 we report the time evolution of $\mathcal{E}$ (as defined above) for the case with $A = 0.5$ [black line, (1)] and $A = 0.2$ [red line (2)] up to $t = 160$. We point out that decreasing the amplitude of the initial perturbations corresponds to a delay in the exponential growth of the electrostatic fluctuations
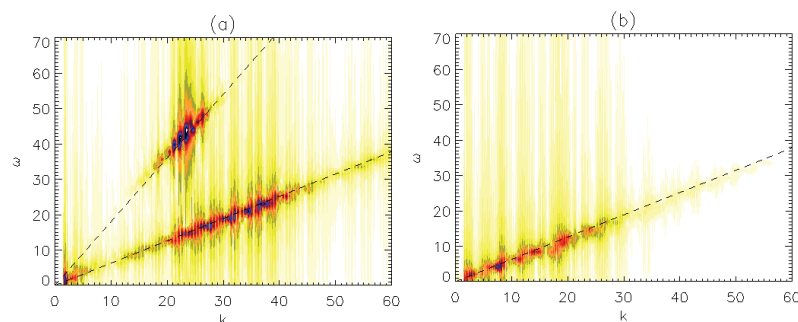

Fig. 15. k-ω spectrum of the parallel electric energy for a simulation with $T_e/T_p = 10$, for $A = 0.5$ (a) and $A = 0.2$ (b).

at small scales and also to a decrease of the growth rate of $\mathcal{E}$. Moreover, the saturation level of $\mathcal{E}$ results about two orders of magnitude lower for $A = 0.2$ with respect to $A = 0.5$. Except for the differences discussed above, Fig. 14 would suggest that the system dynamics is qualitatively similar for both cases $A = 0.2$ and $A = 0.5$; nevertheless, analyzing in more detail the numerical results, we realized that this is not true.

In Fig. 15 we show the k-ω spectra of the longitudinal electric energy for the two simulations with $T_e/T_p = 10$ and $A = 0.5$ (a) and $A = 0.2$ (b). As already shown by Valentini et al. (2008)), for $A = 0.5$ we distinguish two different branches of acoustic waves, the IA waves (upper branch) and the IBk waves (lower branch). The upper dashed line in the top plot of Fig. 15 represents the theoretical prediction for the ion-sound speed c_s (Krall & Trivelpiece, 1986), while the lower dashed line represents the IBk waves phase speed $v_\phi^{(IBk)} \sim 1.2 v_{tp}$. As we discussed earlier, the IA waves are produced by ponderomotive effects. On the other hand, it is clear from the bottom plot of Fig. 15 that, when decreasing the amplitude of the initial perturbations to the value $A = 0.2$, the branch of the IA waves disappears. This is due to the fact that decreasing the amplitude of the perturbation produces a decrease in the density fluctuations generated through ponderomotive effects, thus making the IA fluctuations too weak to survive against Landau damping.

The numerical results shown in Fig. 15 allow to conclude that the IBk waves represent the main component of the longitudinal electric energy spectrum at short scales. The IA waves can represent an additional ingredient when the amplitude of the perturbations is large enough to allow ponderomotive effects to produce high level density fluctuations, but they disappear in the weak perturbation limit.

3.2 Conclusion

In these sections, we discussed numerical results of hybrid Vlasov-Maxwell simulations of turbulence at short scale in the solar wind. The system dynamics in the tail at short wavelengths of the turbulent cascade is analyzed in terms of the electron to proton temperature ratio. Our numerical results show that the electrostatic activity in the termination at small spatial scalelengths of the energy spectra, also recovered in the solar-wind data from spacecraft, mainly consists of a novel branch of waves, called ion-bulk waves, that propagate with phase speed comparable to the proton thermal velocity along the direction of the ambient magnetic field. The peculiarity of these electrostatic fluctuations is that, at variance with the usual ion-acoustic waves, they do not undergo Landau damping even at low values of the electron to proton temperature ratio, since they are sustained by the presence of diffusive plateaus in the longitudinal proton velocity distribution. We emphasize that this numerical evidence can be of strong impact for the case of the solar-wind plasma, where the ratio between electron and proton temperature is typically of order unity.

From the analysis of the numerical results of our hybrid Vlasov-Maxwell simulations, we also found that in correspondence with the propagation of the ion-bulk waves the proton velocity distribution displays the generation of a field-aligned beam of accelerated particles with mean velocity close to the local Alfvén speed. We point out that the mean velocity of this beam does not depend on the electron to proton temperature ratio and for β_p of order unity, appropriate value for the case of the solar wind, it always remains close to V_A, in agreement with the experimental data from observations. We emphasize that previously proposed mechanisms (Araneda et al., 2008; Matteini et al., 2010), based on the excitation of

IA fluctuations by parametric instability of large scale Alfvén waves, succeeds in reproducing the generation of the field-aligned proton beam at $v \simeq V_A$ for a different range of plasma parameters [large T_e/T_p, low β_p and $(T_e/T_p)\beta_p \simeq 1$].

On the other hand, the mechanism discussed in the present paper, based on the excitation of the electrostatic IBk branch, naturally works in the physical conditions of the interplanetary medium, even for small values of the electron to proton temperature ratio, provided the proton plasma beta is of order unity. These numerical results describe a reliable mechanism to explain the complex phenomenology detected in many solar wind measurements from spacecraft and thus can be of relevant importance in the study of the evolution of solar-wind turbulence towards short wavelengths.

4. References

Alexandrova, O.; Saur, J.; Lacombe, C.; Mangeney, A.; Mitchell, J.; Schwartz, S. J. & Robert, P. (2009). Universality of Solar-Wind Turbulent Spectrum from MHD to Electron Scales. *Phys. Rev. Lett.*, Vol.103, 165003.

Araneda, J. A.; Marsch, E. & Vinas, A. (2008). Proton Core Heating and Beam Formation via Parametrically Unstable Alfvãl'n-Cyclotron Waves. *Phys. Rev. Lett.*, Vol. 100, 125003.

Bale, S. D.; Kellogg, P. J.; Mozer, F. S.; Horbury, T. S. & Reme, H. (2005). Measurement of the Electric Fluctuation Spectrum of Magnetohydrodynamic Turbulence. *Phys. Rev. Lett.*, Vol. 94, 215002.

Borovsky, J. (2006). Eddy viscosity and flow properties of the solar wind: Co-rotating interaction regions, coronal-mass-ejection sheaths, and solar-wind/magnetosphere coupling. *Phys. Plasmas*, Vol. 13, 056505.

Borovsky, J. (2008). Flux tube texture of the solar wind: Strands of the magnetic carpet at 1 AU? *J. Geophys. Res.*, Vol. 113, 08110.

Bruno, R. & Carbone, V. (2005). *Living Rev. Solar Phys.*, Vol. 2, 4.

Bruno, R.; Carbone, V.; Veltri, P.; Pietropaolo, E. & Bavassano, B.(2001). Identifying intermittency events in the solar wind. *Planet. Space Sci.*, Vol. 49, 1201.

Burlaga, L. F. (1968). Micro-Scale Structures in the Interplanetary Medium. *Solar Phys.*, Vol. 4, 67.

Burlaga, L. F. (1969). Directional Discontinuities in the Interplanetary Magnetic Field. *Solar Phys.*, Vol. 7, 54.

Carbone, V.; Veltri, P. & Mageney, A.(1990). Coherent structure formation and magnetic field line reconnection in magnetohydrodynamic turbulence. *Phys. Fluids A*, Vol. 2, 1487.

Carbone, V.; Malara, F. & Veltri, P. (1995). A Model for the Three-Dimensional Magnetic Field Correlation Spectra of Low-Frequency Solar Wind Fluctuations During Alfvãl'nic Periods. *J. Geophys. Res.*, Vol. 100, 1763.

Cassak, P. A. & Shay, M. A. (2007). Scaling of asymmetric magnetic reconnection: General theory and collisional simulations. *Phys. Plasmas*, Vol. 14, 102114.

Daughton, W.; Roytershteyn, V.; Karimabadi, H.; Yin, L.; Albright, B. J.; Bergen, B. & Bowers, K. J. (2011). Role of electron physics in the development of turbulent magnetic reconnection in collisionless plasmas. *Nature Phys.*, Vol. 7, 539.

Dmitruk, P. & Matthaeus, W. H. (2006). Structure of the electromagnetic field in three-dimensional Hall magnetohydrodynamic turbulence. *Phys. Plasmas*, Vol. 13, 042307.

Dobrowolny, M.; Mangeney, A. & Veltri, P. (1980). Properties of magnetohydrodynamic turbulence in the solar wind. *Astron. Astrophys.*, Vol. 83, 26.

Dungey, J. W. (1958). *Cosmic Electrodynamics*, Cambridge University Press, England.

Gosling, J. T. & Szabo, A. (2008). Bifurcated current sheets produced by magnetic reconnection in the solar wind, *J. Geophys. Res.*, Vol. 113, A10103.

Greco, A.; Chuychai, P.; Matthaeus, W. H.; Servidio, S. & Dmitruk, P. (2008). Intermittent MHD structures and classical discontinuities, *Geophys. Res. Lett.*, Vol. 35, L19111.

Greco, A.; Matthaeus, W. H.; Servidio, S.; Chuychai, P. & Dmitruk, P. (2009). Statistical Analysis of Discontinuities in Solar Wind ACE Data and Comparison with Intermittent MHD Turbulence. *Astrophys. J.*, Vol. 691, L111.

Gurnett, D. A. & Andreson, R. R. (1977). Plasma Wave Electric Fields in the Solar Wind: Initial Results From Helios 1. *J. Geophys. Res.*, Vol. 82, 632.

Gurnett, D. A. & Frank, L. A. (1978). Ion Acoustic Waves in the Solar Wind, *J. Geophys. Res.*, Vol. 83, 58.

Gurnett; D. A., Marsch, E.; Pilipp, W.; Schwenn, R. & Rosenbauer, H. (1979). Ion Acoustic Waves and Related Plasma Observations in the Solar Wind. *J. Geophys. Res.*, Vol. 84, 2029.

Hada, T.; Koga, D. & Yamamoto, E. (2003). Phase coherence of MHD waves in the solar wind. *Space Sci. Rev.*, Vol. 107, 463.

Hellinger, P.; TravnÄścek, P.; Kasper, J. C. & Lazarus, A. J. (2006). Solar wind proton temperature anisotropy: Linear theory and WIND/SWE observations. *Geophys. Res. Lett.*, Vol. 33, L09101.

Heuer, M. & Marsch, E. (2007). Diffusion plateaus in the velocity distributions of fast solar wind protons. *J. Geophys. Res.*, Vol. 112, A03102.

Holloweg, J. V. & Isenberg, P. A. (2002). Generation of the fast solar wind: A review with emphasis on the resonant cyclotron interaction. *J. Geophys. Res.*, Vol. 107, 1147.

Howes, G. G; Dorland, W.; Cowley, S. C.; Mammet, G. W.; Quataert, E.; Schekochihin, A. A. & Tatsuno, T. (2008). Kinetic Simulations of Magnetized Turbulence in Astrophysical Plasmas. *Phys. Rev. Lett.*, Vol. 100, 065004.

Koga, D.; Chian, A. C.-L.; Miranda, R. A. & Rempel, E. L. (2007). Intermittent nature of solar wind turbulence near the Earth's bow shock: Phase coherence and non-Gaussianity. *Phys. Rev. E*, Vol. 75, 046401.

Koga, D. & Hada, T. (2003). Phase coherence of foreshock MHD waves: wavelet analysis. *Space Sci. Rev.*, Vol. 107, 495.

Kennel, C. F. & Engelmann, F. (1966). *Phys. Fluids*, Vol. 9, 2377.

Krall, N. A. & Trivelpiece, A. W. (1986). *Principles of plasma physics*, San Francisco Press, San Francisco.

Lacombe C.; Salem, C.; Mangeney, A.; Hubert, D.; Perche, C.; Bougeret, J.-L.; Kellogg, P. J. & Bosqued, J.-M. (2002). Evidence for the interplanetary electric potential? WIND observations of electrostatic fluctuations. *Ann. Geophys.*, Vol. 20, 609.

Lapenta, G. (2008). Self-Feeding Turbulent Magnetic Reconnection on Macroscopic Scales. *Phys. Rev. Lett.*, Vol. 100, 235001.

Leamon, R. J.; Matthaeus, W. H.; Smith, C. W.; Zank, G.P.; Mullan, D. J. & and Oughton, S. (2000). MHD-driven Kinetic Dissipation in the Solar Wind and Corona. *Astrophys. J.*, Vol. 537, 1054.

Longtin, M. & Sonnerup, B. U.O. (1986). Modulation Instability of Circularly Polarized AlfvÃľn Waves. *J. Geophys. Res.*, Vol. 91, 6816.

Malara, F.; Veltri, P. & Carbone, V. (1992). Competition among nonlinear effects in tearing instability saturation. *Phys. Fluids B*, Vol. 4, 3070.

Mangeney A.; Salem, C.; Lacombe, C.; Bougeret, J.-L.; Perche, C.; Manning, R.; Kellogg, P. J.; Goetz, K.; Monson, S. J. & Bosqued, J.-M. (1999). WIND observations of coherent electrostatic waves in the solar wind. *Ann. Geophys.*, Vol. 17, 307.

Marsch, E.; Muhlhauser, K.-H.; Schwenn, R.; Rosenbauer, H.; Pilipp, W. & Neubauer, F. (1982). Solar Wind Protons: Three-Dimensional Velocity Distributions and Derived Plasma Parameters Measured Between 0.3 and 1 AU. *J. Geophys. Res.*, Vol. 87, 52.

Marsch, E.; Ao, X.-Z. & Tu, C.-Y. (2004). On the temperature anisotropy of the core part of the proton velocity distribution function in the solar wind. *J. Geophys. Res.*, 109, A04102.

Matteini, L., Landi, S., Velli, M., & Hellinger, P. (2010), Kinetics of parametric instabilities of AlfvÃl'n waves: Evolution of ion distribution functions, *J. Geophys. Res.*, Vol. 115, A09106.

Matthaeus, W. H. & and Montgomery, D. (1980). Selective decay hypothesis at high mechanical and magnetic Reynolds numbers. *Ann. N.Y. Acad. Sci.*, Vol. 357, 203.

Matthaeus, W. H. & Lamkin, S. L. (1986). Turbulent magnetic reconnection. *Phys. Fluids*, Vol. 29, 2513.

Matthaeus, W. H.; Goldstein, M. L. & King, J. H. (1986). An Interplanetary Magnetic Field Ensemble at 1 AU. *J. Geophys. Res.*, Vol. 91, 59.

Mininni, P. D. & Pouquet, A. (2009). Finite dissipation and intermittency in magnetohydrodynamics. *Phys. Rev. E*, Vol. 80, 025401.

Moffatt, H. K. (1978). *Magnetic field generation in electrically conducting fluids*, Cambridge U. Press, Cambridge, England.

Ness, N. F. & Burlaga, L. F. (2001). Spacecraft studies of the interplanetary magnetic field. *J. Geophys. Res.*, Vol. 106, 15803.

Neugebauer, M. (2006). Comment on the abundances of rotational and tangential discontinuities in the solar wind. *J. Geophys. Res.*, Vol. 111, A04103.

Osman, K. T.; Matthaeus, W. H.; Greco, A. & Servidio, S. (2011). Evidence for Inhomogeneous Heating in the Solar Wind, *Astrophys. J.*, Vol. 727, L11.

Parker, E. N. (1957). Sweet's Mechanism for Merging Magnetic Fields in Conducting Fluids. *J. Geophys. Res.*, Vol. 62, 509.

Parker, E. N. (1983). Magnetic neutral sheets in evolving fields. Formation of the solar corona. *Astrophys. J.*, Vol. 264, 642.

Phan, T. D.; Gosling, J. T.; Paschmann, G.; Pasma, C.; Drake, J. F.; Oieroset, M.; Larson, D.; Lin, R. P. & Davis, M. S. (2010). The Dependence of Magnetic Reconnection on Plasma Îš and Magnetic Shear: Evidence from Solar Wind Observations. *Astrophys. J.*, Vol. 719, L199.

Pickett J. S.; Chen, L.-J.; Kahler, S. W.; Santolík, O.; Gurnett, D. A.; Tsurutani, B. T. & Balogh, A. (2004). Isolated electrostatic structures observed throughout the Cluster orbit: relationship to magnetic field strength. *Ann. Geophys.*, 22, 2515.

Priest, E. R. & Pontin, D. I. (2009). Three-dimensional null point reconnection regimes. *Phys. Plasmas*, Vol. 16, 122101.

Ren, Y.; Yamada, M.; Gerhardt, S.; Ji, H.; Kulsrud, R & Kuritsyn, A. (2005). Experimental Verification of the Hall Effect during Magnetic Reconnection in a Laboratory Plasma. *Phys. Rev. Lett.*, Vol. 95, 055003.

Retinò, A.; Sundkvist, D.; Vaivads, A.; Mozer, F.; André, M. & Owen, C. J. (2007). In situ evidence of magnetic reconnection in turbulent plasma, *Nature Phys.*, Vol. 3, 236.

Sahraoui, F.; Goldstein, M. L.; Robert, P.; & Khotyaintsev, Yu. V. (2009). Evidence of a Cascade and Dissipation of Solar-Wind Turbulence at the Electron Gyroscale. *Phys. Rev. Lett.*, Vol. 102, 231102.

Sahraoui, F. & and Goldstein, M. (2010). Structures and Intermittency in Small Scales Solar Wind Turbulence, *Twelfth International Solar Wind Conference, AIP Conference Proceedings*, Vol. 1216, 140, Saint-Malo, France, 21-26 June 2009.

Schwenn, R. & Marsch, E. (1991). *Physics of the Inner Heliosphere II. Particles, Waves and Turbulence*, Vol. 2, Springer.

Servidio, S.; Matthaeus; W. H. & Dmitruk, P. (2008). Depression of Nonlinearity in Decaying Isotropic MHD Turbulence. *Phys. Rev. Lett.*, Vol. 100, 095005.

Servidio, S.; Matthaeus, W. H.; Shay, M. A.; Cassak, P. A. & Dmitruk, P. (2009). Magnetic Reconnection in Two-Dimensional Magnetohydrodynamic Turbulence. *Phys. Rev. Lett.*, Vol. 102, 115003.

Servidio, S.; Matthaeus, W. H.; Shay, M. A.; Dmitruk, P.; Cassak, P. A. & Wan, M. (2010). Statistics of magnetic reconnection in two-dimensional magnetohydrodynamic turbulence. *Phys. Plasmas*, Vol. 17, 032315.

Servidio, S.; Wan, M.; Matthaeus, W. H. & Carbone, V. (2010). Local relaxation and maximum entropy in two-dimensional turbulence. *Phys. Fluids*, Vol. 22, 125107.

Servidio, S.; Greco, A.; Matthaeus, W. H.; Osman, K. T. & Dmitruk, P. (2011). Statistical association of discontinuities and reconnection in magnetohydrodynamic turbulence. *J. Geophys. Res.*, Vol. 116, A09102.

Sonnerup, B. U. O. & Cahill, L. J. (1967). Magnetopause Structure and Attitude from Explorer 12 Observations. *J. Geophys. Res.*, Vol. 72, 171.

Sonnerup, B. U. O.; Paschmann, G.; Papamastorakis, I.; Sckopke, N.; Haerendel, G.; Bame, S. J.; Asbridge, J. R.; Gosling, J. T & Russel, C. T. (1981). Evidence for Magnetic Field Reconnection at the Earth's Magnetopause. *J. Geophys. Res.*, Vol. 86, 10049.

Sweet, P. A. .(1958). *Electromagnetic Phenomena in Cosmical Physics*, Cambridge University Press, New York.

Sundkvist, D.; Retino, A.; Vaivads A. & Bale, S. D. (2007). Dissipation in Turbulent Plasma due to Reconnection in Thin Current Sheets. *Phys. Rev. Lett.*, Vol. 99, 025004.

Tsurutani, B. T. & Smith, E. J. (1979). Interplanetary discontinuities - Temporal variations and the radial gradient from 1 to 8.5 AU. *J. Geophys. Res.*, Vol. 84, 2773.

Tu, C. -Y; Marsch, E. & Qin, Z.-R. (2004). Dependence of the proton beam drift velocity on the proton core plasma beta in the solar wind. *J. Geophys. Res.*, Vol. 109, A05101.

Valentini F.; Travnicek, P.; Califano, F.; Hellinger, P. & Mangeney, A. (2007). A hybrid-Vlasov model based on the current advance method for the simulation of collisionless magnetized plasma. *J. Comput. Phys. 225*, Vol. 753.

Valentini, F.; Veltri, P.; Califano, F. & Mangeney, A. (2008). Cross-Scale Effects in Solar-Wind Turbulence. *Phys. Rev. Lett.*, Vol. 101, 025006.

Valentini, F. & Veltri, P. (2009). Electrostatic Short-Scale Termination of Solar-Wind Turbulence. *Phys. Rev. Lett.*, Vol. 102, 225001.

Valentini, F.; Califano, F. & Veltri, P. (2010). Two-Dimensional Kinetic Turbulence in the Solar Wind. *Phys. Rev. Lett.*, Vol. 104, 205002.

Valentini, F.; Califano, F.; Perrone, D.; Pegoraro, F. & Veltri, P. (2011). New Ion-Wave Path in the Energy Cascade. *Phys. Rev. Lett.*, Vol. 106, 165002.

Vasquez, B. J.; Abramenko, V. I.; Haggerty, D. K & Smith, C. W. (2007). Numerous small magnetic field discontinuities of Bartels rotation 2286 and the potential role of AlfvÃl'nic turbulence. *J. Geophys. Res.*, Vol. 112, 11102.

Veltri, P. (1999). MHD turbulence in the solar wind: self-similarity, intermittency and coherent structures, *Plasma Phys. Control. Fusion*, Vol. 41, A787.

Veltri, P. & and Mangeney, A. (1999). Scaling laws and intermittent structures in solar wind MHD turbulence, *Solar Wind IX, AIP Conference Proceedings*, Vol. 471, 543. Nantucket Island (Massachusetts, USA), 5-9 October, 1999.

Wan, M.; Oughton, S.; Servidio, S. & Matthaeus, W. H. (2010). On the accuracy of simulations of turbulence, *Phys. Plasmas*, Vol. 17, 082308.
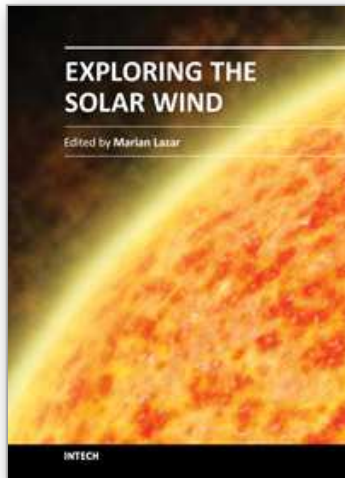
Exploring the Solar Wind

Edited by Dr. Marian Lazar

This book consists of a selection of original papers of the leading scientists in the fields of Space and Planetary Physics, Solar and Space Plasma Physics with important contributions to the theory, modeling and experimental techniques of the solar wind exploration. Its purpose is to provide the means for interested readers to become familiar with the current knowledge of the solar wind formation and elemental composition, the interplanetary dynamical evolution and acceleration of the charged plasma particles, and the guiding magnetic field that connects to the magnetospheric field lines and adjusts the effects of the solar wind on Earth. I am convinced that most of the research scientists actively working in these fields will find in this book many new and interesting ideas.

How to reference

In order to correctly reference this scholarly work, feel free to copy and paste the following:

INTECH
open science | open minds